chemosensors

MDPI

Article

Batch-Injection Amperometric Determination of Glucose Using a $NiFe_2O_4$/Carbon Nanotube Composite Enzymeless Sensor

Amanda B. Nascimento [1], Lucas V. de Faria [1,2], Tiago A. Matias [1,3], Osmando F. Lopes [1] and Rodrigo A. A. Muñoz [1,*]

[1] Institute of Chemistry, Federal University of Uberlândia, Uberlândia 38400-902, MG, Brazil; amandabnascimento842@gmail.com (A.B.N.); lucasviniciusfaria@gmail.com (L.V.d.F.); tiago.matias@ufes.br (T.A.M.); osmando@ufu.br (O.F.L.)
[2] Institute of Chemistry, Department of Analytical Chemistry, Fluminense Federal University, Niteroi 24020-141, RJ, Brazil
[3] Chemistry Department, Federal University of Espírito Santo—UFES, Vitória 29075-910, ES, Brazil
* Correspondence: munoz@ufu.br

Abstract: The development of sensitive and selective analytical devices for monitoring glucose levels (GLU) in biological fluids is extremely important for clinical diagnostics. In this work, we produced a new composite based on $NiFe_2O_4$ and multi-walled carbon nanotubes (MWCNT), called $NiFe_2O_4$@MWCNT, to be applied as a non-enzymatic amperometric sensor for GLU. Both $NiFe_2O_4$ and $NiFe_2O_4$@MWCNT composites were properly characterized by XRD, SEM, FTIR, and Raman spectroscopy, which confirmed that the composite was successfully prepared. A glassy-carbon electrode (GCE) modified with $NiFe_2O_4$@MWCNT was investigated by cyclic voltammetry and applied for the amperometric GLU detection using batch-injection analysis (BIA). A linear working range between 50 and 600 μmol L^{-1} GLU with a significant increase in sensitivity (3-fold) in comparison with MWCNT/GCE was verified, with a detection limit of 36 μmol L^{-1}. Inter-electrode measurements (n = 4, RSD = 10%) indicated that the sensor fabrication is reproducible. Furthermore, the proposed non-enzymatic sensor was selective even in the presence of other biomarkers found in urine. When applied to synthetic urine samples, recovery levels between 84 and 95% confirmed analytical accuracy and the absence of sample matrix effect. Importantly, the developed approach is simple (free of biological modifiers), fast (77 injections per hour), and practical (high-performance tool), which are suitable features for routine analyses.

Keywords: ferrites; enzymeless; glucometer; amperometric detection; nanocomposite

check for updates

Citation: Nascimento, A.B.; de Faria, L.V.; Matias, T.A.; Lopes, O.F.; Muñoz, R.A.A. Batch-Injection Amperometric Determination of Glucose Using a $NiFe_2O_4$/Carbon Nanotube Composite Enzymeless Sensor. *Chemosensors* **2024**, *12*, 112. https://doi.org/10.3390/chemosensors12060112

Received: 2 May 2024
Revised: 11 June 2024
Accepted: 14 June 2024
Published: 16 June 2024

Correction Statement: This article has been republished with a minor change. The change does not affect the scientific content of the article and further details are available within the backmatter of the website version of this article.

Copyright: © 2024 by the authors. Licensee MDPI, Basel, Switzerland. This article is an open access article distributed under the terms and conditions of the Creative Commons Attribution (CC BY) license (https://creativecommons.org/licenses/by/4.0/).

1. Introduction

Diabetes Mellitus (DM) is one of the most common diseases in the world, and its diagnosis is based on the detection of glucose (GLU) in biological fluids, such as urine, saliva, and blood [1]. As diabetes is a chronic disease, the level of glucose in biological fluids needs to be measured frequently to ensure patient health, and this control can be performed by colorimetric [2] and electrochemical methods [3]. Electrochemical methods are mostly used because they offer quick response, high sensitivity, stability, and a simple operation process [3,4].

The first enzymatic sensor for GLU was developed in 1960 [4], and this type of sensor is the principal method for determining GLU. These sensors are based on an enzymatic reaction, mainly using glucose oxidase (GOx) that reacts with GLU, generating gluconic acid and hydrogen peroxide, involving the consumption of oxygen [5–7]. Monitoring either oxygen consumption or generated products by an electrochemical method enables indirect GLU sensing [4,8]. However, enzymatic sensors present disadvantages, such as low stability, difficulty in storage, and dependence on temperature, pH, and humidity, which decrease the enzyme's catalytic activity [9]. For this reason, non-enzymatic sensors

for GLU detection are gaining attention, and their development has increased exponentially due to advancements in nanotechnology.

Different nanomaterials have been employed as electrode modifiers to provide selective and sensitive GLU sensors. Metal oxides [10] and hydroxides [11], transition metals [12], metal-organic framework (MOF) derived materials [13], spinel cobaltite [14], and ferrite materials [15] have been investigated in the development of electrochemical sensors for GLU. Nickel-based materials have shown interesting features for GLU detection because the analyte interacts with Ni^{2+}, becoming adsorbed on the $Ni(OH)_2$ surface, which is the first step of the process in the formation of the $NiOOH/Ni(OH)_2$ pair, responsible for the GLU oxidation in alkaline medium [16,17].

Spinel ferrites have been recently highlighted as a new class of materials with great potential for electrochemical sensing [18,19]. On the other hand, spinel ferrites showed powerful catalytic properties for the detection of target species in biological matrices without requiring the combination with enzymes or other biological agents [20]. They offer additional advantages, including biocompatibility, low production cost, low toxicity, high conductivity, and ferromagnetic properties [21–23]. Moreover, $NiFe_2O_4$ presents a stable crystalline phase, which increases the stability of the material during the synthesis and application. This is a crucial advantage when compared to other materials, such as $Ni(OH)_2$, in the development of non-enzymatic sensors for GLU. The $Ni(OH)_2$ species can present an unstable phase that may affect the sensor stability. Furthermore, $NiFe_2O_4$ also presents a fast charge transfer process due to the presence of Ni^{+2} and Fe^{3+} in octahedral and tetrahedral sites. This organization facilitates electron transfer because it occurs through a hopping process [24].

In this context, one strategy to develop high-performance electrochemical sensors involves the association of different inorganic materials, like those previously mentioned, with carbon nanomaterials to enhance the sensing properties towards the detection of several analytes, including GLU [16]. The formation of composites with carbon nanomaterials improves catalyst stability and generates a more homogenous distribution of the catalyst on the modified substrate, which proportionally improves sensing properties due to better access to the catalyst sites. Moreover, carbon nanomaterials, such as carbon nanotubes (CNTs), present high electrical conductivity that improves the charge transfer constant, which can lead to the development of enhanced sensors [25].

Electrochemical studies using composites of spinel ferrites with CNTs or other carbon-based nanomaterials as modifying agents have been applied for sensing various molecules using mainly voltammetric techniques [22,26–28]. However, an interesting technique for monitoring GLU is amperometry [29], which can be easily coupled to high-throughput analytical systems, such as batch-injection analysis (BIA) [30,31]. The BIA system provides fast, sensitive, low cost and portable analysis [30]. Because of these features, BIA has been employed as a powerful analytical tool for the determination of environmental and clinical molecules [32,33]. Moreover, the association of BIA with a non-enzymatic sensor can provide a promising analytical approach for GLU sensing, especially using $NiFe_2O_4$, a material with admirable electrochemical properties [6].

Herein, we demonstrate that a composite formed by $NiFe_2O_4$ and multi-walled CNTs (MWCNTs) can be easily immobilized on a glassy-carbon electrode (GCE) surface by drop-casting, and the modified electrode presents outstanding amperometric sensing properties for GLU. First, we present the step-by-step electrode construction and its characterization, which guided us in the development of this enzymeless GLU sensor. Nickel ferrites were one-pot synthesized by a hydrothermal method, then combined with MWCNTs, and then immobilized on a GCE surface. The electrode was coupled to a batch-injection cell for amperometric GLU sensing. Batch-injection analysis with amperometric detection (BIA-AD) was selected due to its practicability and ease of implementation in routine analyses [30]. The high-speed injection provided by an electronic micropipette provides increased sensitivity in comparison with steady-state amperometric measurements [34].

2. Materials and Method

2.1. Reagents, Solutions, and Samples

Highly pure deionized water (R $\geq$ 18 MΩ cm) obtained from a Millipore Direct-Q3 system (Bedford, MA, USA) was used to prepare all aqueous solutions. Iron nitrate nonahydrate (98% *w*/*w*), MWCNTs (95% *w*/*w*) and uric acid (99% *w*/*w*) were purchased from Sigma-Aldrich (Steinheim, Germany), nickel nitrate heptahydrate (97% *w*/*w*), sodium hydroxide (85% *w*/*w*) and urea (99% *w*/*w*) from Dinamica (São Paulo, Brazil), trisodium citrate and ascorbic acid from Malinckrodt (St. Louis, USA) and GLU (99.5% *w*/*w*) from Henrifarma (São Paulo, Brazil).

The standard solutions of GLU, urea, ascorbic acid, and uric acid were prepared in supporting electrolytes (1.0 mol L^{-1} NaOH). The synthetic urine was prepared as reported by Brooks and Keevil [35], which contains citric acid (2.1 mmol L^{-1}), uric acid (0.4 mmol L^{-1}), urea (166.5 mmol L^{-1}), sodium bicarbonate (25.0 mmol L^{-1}), calcium chloride (0.4 mmol L^{-1}), sodium chloride (89.0 mmol L^{-1}), sodium sulfate (9.9 mmol L^{-1}), magnesium sulfate (4.1 mmol L^{-1}), ammonium chloride (24.3 mmol L^{-1}), ammonium chloride (24.3 mmol L^{-1}), sodium nitrite (0.7 mmol L^{-1}), and disodium phosphate (9.0 mmol L^{-1}). The pH value of this synthetic urine sample was approximately 6.4.

2.2. Synthesis and Characterization of $NiFe_2O_4$

$NiFe_2O_4$ samples were synthesized using the hydrothermal coprecipitation method based on the work of Kurian et al. (2021) [36]. For synthesis, $Fe(NO_3)_3.9H_2O$ (20 mmol L^{-1}) and $Ni(NO_3)_2.5H_2O$ (10 mmol L^{-1}) were used in proportion 2:1, respectively, in 100 mL deionized water. Trisodium citrate (0.15 mol L^{-1}) and NaOH (2 mol L^{-1}) were also used as surfactant and precipitant agents, respectively. The precursors $Fe(NO_3)_3.9H_2O$ and $Ni(NO_3)_2.5H_2O$ were added to the Teflon cup with deionized water and kept under constant stirring for 5 min. After, trisodium citrate was added, and the solution was kept under constant stirring for 15 min. After this time, the NaOH solution was added until the solution pH reached 12.0. This final solution was transferred to a Teflon-lined stainless steel autoclave and kept at 200 °C for 16 h. The obtained material was washed with water and isopropyl alcohol, centrifuged, and dried for 24 h at 70 °C in a stove.

The crystalline phase of $NiFe_2O_4$ was investigated by X-ray diffractometry (XRD) collected in a Shimadzu XRD6000 diffractometer (40 kV, 30 mA) with CuKα radiation (λ = 1.5418 Å). The measurements were made at a scan rate of 0.5° min^{-1} and 2θ angles between 10° and 70°. The morphology of $NiFe_2O_4$ samples was investigated by scanning electron microscopy (SEM) images collected in a Tescan VEJA 3 LMU microscope operating at 10 kV. The materials were also investigated by Energy-dispersive spectroscopy (EDS) using an Oxford detector (model INSCA X-CTA). The $NiFe_2O_4$ samples were evaluated by Fourier-transform infrared spectroscopy (FTIR) with a PerkinElmer spectrometer, model Spectrum Two, in attenuated total reflectance (ATR) mode with a CsI detector. Measurements were performed using 16 cycles from 500 to 4000 cm^{-1}. The $NiFe_2O_4$@MWCNT composite was also characterized by Raman spectroscopy with a HORIBA spectrometer, model LabRAM HR Evolution, and an OSD Syncerity detector. The measurements were made with a laser set at 532 nm.

2.3. Preparation of $NiFe_2O_4$@MWCNTs Suspension and Modification of the GCE Surface

The suspension was prepared by dispersing 5 mg of MWCNT in dimethylformamide (DMF) using an ultrasonic tip of high frequency for 15 min, and after this, 5 mg of $NiFe_2O_4$ was added, and the suspension was sonicated again for 15 min. Before modification, the GCE surface was polished in alumina slurry. Subsequently, the GCE surface was modified with 10 μL of the $NiFe_2O_4$@MWCNTs suspension and dried in a stove for 30 min at 50 °C. After drying, the electrode surface was washed with water, and the electrode was ready for use.

2.4. Electrochemical Measurements

All electrochemical measurements (cyclic voltammetry (CV) and BIA-AD) were performed with a μ-AUTOLAB type III AUT85340 potentiostat/galvanostat (Metrohm Autolab BV, Utrecht, The Netherlands) controlled by Nova 2.4. software. The electrochemical analysis was conducted at room temperature (26 ± 2 °C) in the presence of dissolved oxygen using 1.0 mol L^{-1} NaOH solution (pH 14) as the supporting electrolyte. The BIA-AD analysis was performed in a BIA-cell (internal volume of 200 mL) with a working electrode in wall-jet configuration, in which the injections were made using an Eppendorf electronic micropipette (multipette® E3) at a programmable dispensing rate. No stirring of the solution was required during the amperometric measurements. In both experiments (CV and BIA-AD), a miniaturized Ag | AgCl | $KCl_{(sat.)}$ and platinum wire electrode were used as the reference and auxiliary electrodes, respectively. The working electrode was an unmodified GCE disc (6.5 mm diameter) and modified with the $NiFe_2O_4$/MWCNTs suspension ($NiFe_2O_4$@MWCNTs/GCE).

3. Results and Discussion

3.1. Characterization of $NiFe_2O_4$ and $NiFe_2O_4$@MWCNT Composite

The FTIR spectra of $NiFe_2O_4$ and MWCNT samples are shown in Figure 1A. The spectrum of $NiFe_2O_4$ reveals a band at 556 cm^{-1} that corresponds to the Fe-O bond in the tetrahedral site, which is characteristic of $NiFe_2O_4$ [37]. The bands at 1363 and 1578 cm^{-1} correspond to the carboxyl (COO^-) group from metallic carboxylates [38,39]. The band at 1363 cm^{-1} corresponds to the asymmetric vibration of the C-O bond, and the band at 1578 cm^{-1} corresponds to the symmetric vibration of the C=O bond. The presence of these bands is explained by the formation of complexes between metal ions and citrate during the synthesis process [38,39]. The band at 3359 cm^{-1} corresponds to the O-H bond of water. The hydrothermal method is characterized by the reaction in the presence of water as the solvent. Therefore, the presence of an O-H bond is attributed to the solvent used in the synthesis. During the hydrothermal reaction with the coprecipitation method, the reaction mechanism is divided into three phases. The first step is the formation of complexes between metallic ions (Fe^{3+} and Ni^{2+}) and citrate, forming metallic complexes. This step occurs during the coprecipitation method, before the hydrothermal reaction. These complexes are decomposed during the hydrothermal reaction at high temperatures, forming hydroxides, characterizing the second step of the reaction [38,39]. The third step is the conversion of hydroxide to nickel ferrite. Therefore, the presence of peaks assigned to the carbon species can be related to residual species from the synthesis that were not decomposed during the reaction process.

The FTIR spectrum of MWCNT exhibits characteristic bands indicative of functionalized materials. The features observed at 3402 and 3275 cm^{-1} indicate the presence of O-H stretching attributed to the carboxylic groups. The features observed at 1606 and 1098 cm^{-1} correspond to C=O and C-O stretching, respectively, which can also be attributed to the carboxylic groups. Moreover, it is possible to notice typical features of MWCNT at 1521 and 1098 cm^{-1} corresponding to C=C stretching and -CH bend vibration, respectively [40,41].

The $NiFe_2O_4$ sample was characterized by X-ray diffraction to confirm the crystalline phase of the material and its crystallinity. Figure 1C shows the diffractogram that shows the peaks at 18.47° (111), 30.35° (220), 35.65° (311), 37.30° (222), 43.37° (400), 57.39° (511), and 63.08° (440) [42]. These peaks can be related to the cubic phase of the $NiFe_2O_4$ (PDF 86-2267), with space group Fd-3m (no. 227). The crystallite size was calculated by the Scherrer equation, and the value of 5.5 nm was found. Furthermore, the absence of characteristic peaks of NiO and FeO reveals that the material does not contain impurities or a phase mixture. The intensity and profile of peaks are the results of the high temperature used in the synthesis because they offer energy for the rearrangement of atoms in the crystal lattice, resulting in more defined crystallographic planes [43,44]. Therefore, we can conclude that the hydrothermal treatment was efficient in obtaining the $NiFe_2O_4$ samples with high crystallinity.

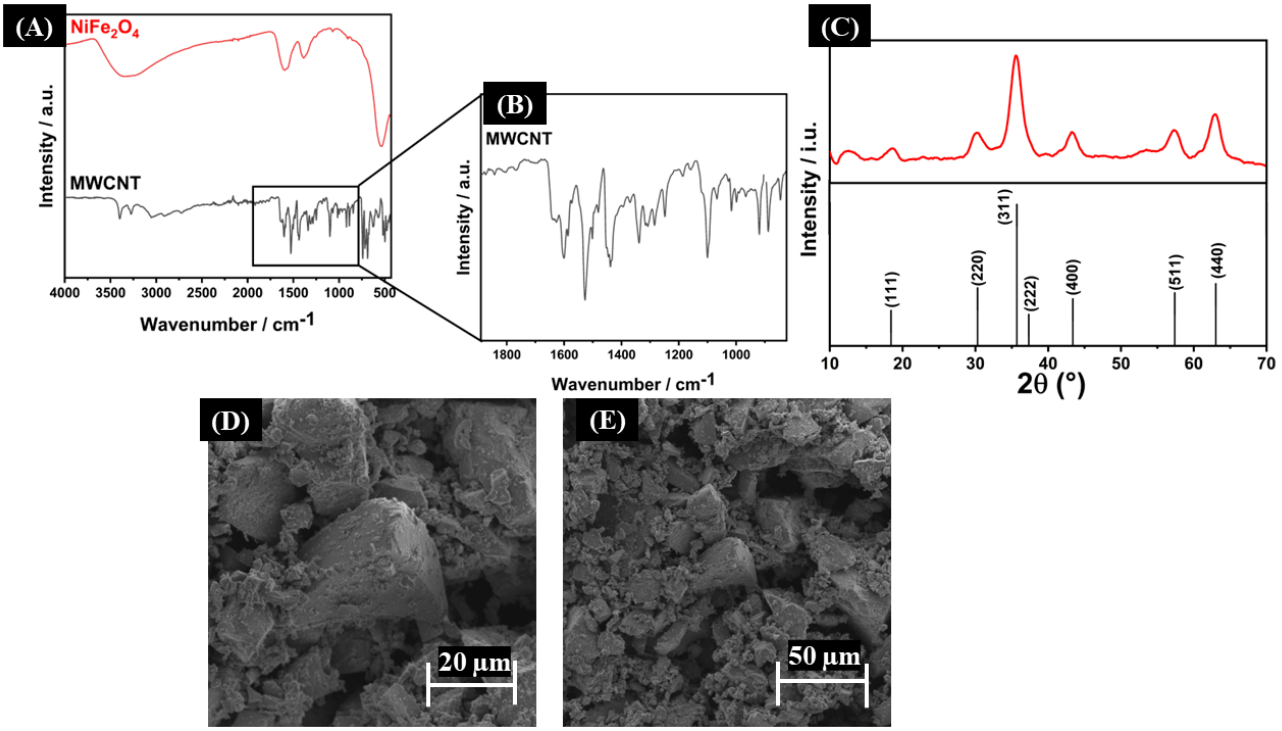

Figure 1. (**A**) FTIR spectra of MWCNT (black line) and $NiFe_2O_4$ (red line); (**B**) Amplified FTIR spectrum of MWCNT; (**C**) XRD patterns of synthesized $NiFe_2O_4$ through coprecipitation method with hydrothermal treatment at 200 °C for 16 h; (**D**,**E**) SEM images of $NiFe_2O_4$ synthesized by 200 °C for 16 h.

The sample's morphology of $NiFe_2O_4$ was analyzed by SEM (Figure 1D,E). The image shows particles with different sizes and morphology. The lack of uniformity of the material is associated with the growth and nucleation process that dictates the morphological characteristics and size of the materials synthesized by the hydrothermal method [45,46]. The growth and nucleation processes influence the morphology and size of particles because during the synthesis process, the first step is nucleation, which influences the size of particles, and the second step is the growth process that occurs by mass transfer [46]. In this way, the difference in the size of $NiFe_2O_4$ particles occurs because the mass transfer is uneven throughout the synthesis process. Moreover, Figure 1D shows that the particles are agglomerated due to the interactions between the magnetic dipoles of the material [47,48]. This behavior is common due to the ferromagnetic properties of the materials [49]. Figure S1A presents the SEM image of the $NiFe_2O_4$@MWCNT composite, which shows large $NiFe_2O_4$ particles and some agglomerated particles spread over the MWCNT structure (the presence of MWCNT is not clear in the composite because of the difference in scale resolution as $NiFe_2O_4$ particles are much larger than MWCNTs). This behavior is confirmed by analyzing the separate images of $NiFe_2O_4$ (Figure 1D) and MWCNT (Figure S1B). Figure S1B presents the SEM image of MWCNT, which presents the well-known morphology of interconnected tubular structures ("spaghetti-like structure") [50,51].

An EDS analysis was performed to confirm the presence of nickel, iron, oxygen, and carbon in synthesized materials. Figure S2 presents the spectra for the $NiFe_2O_4$, MWCNT, and $NiFe_2O_4$@MWCNT composite, respectively. These spectra confirmed the presence of common elements in these materials. Figure S2C reveals the presence of carbon from the MWCNT as well as the presence of nickel and iron from $NiFe_2O_4$.

Furthermore, the structure of $NiFe_2O_4$@MWCNT composite was characterized by Raman spectroscopy. Figure 2 displays the Raman spectra for MWCNT (black line), $NiFe_2O_4$ (red line), and $NiFe_2O_4$@MWCNT (blue line). The MWCNT spectrum presents bands at 1340, 1576, and 2600 cm^{-1} that correspond to D, G, and 2D bands, respectively [52]. The D

band is related to the carbon bond and the loss of symmetry of the graphene lattice due to the carbonaceous impurities with sp^3 bonds and broken sp^2 bonds at the sidewalls. The G band refers to carbons with sp^2 hybridization [52]. The 2D band also corresponds to carbons with sp^2 hybridization, and your intensity is proportional to the number of walls in graphene [53,54]. The $NiFe_2O_4$ spectrum presents five bands at 330, 485, 558, 692, and 1340 cm^{-1}, with symmetry E_g, $T_{2g(1)}$, $T_{2g(2)}$, $A_{1g(1)}$, and $A_{1g(2)}$, respectively [55]. The bands of 330 to 558 cm^{-1} correspond to the metal-oxygen bond (Fe-O) in the octahedral site [55], while the band at 692 cm^{-1} refers to the metal-oxygen bond (Fe-O) in the tetrahedral site [56]. Therefore, the bands at lower wave numbers are related to metal-oxygen bonds in octahedral sites, whereas the bands at high wave numbers are related to metal-oxygen bonds in tetrahedral sites. The band at 1340 cm^{-1} corresponds to the presence of the carboxyl group (COO^-) [57], which was also verified by FTIR. The $NiFe_2O_4$@MWCNT spectrum presents all bands referring to $NiFe_2O_4$ and MWCNT, confirming the presence of these materials in the synthesized composite.

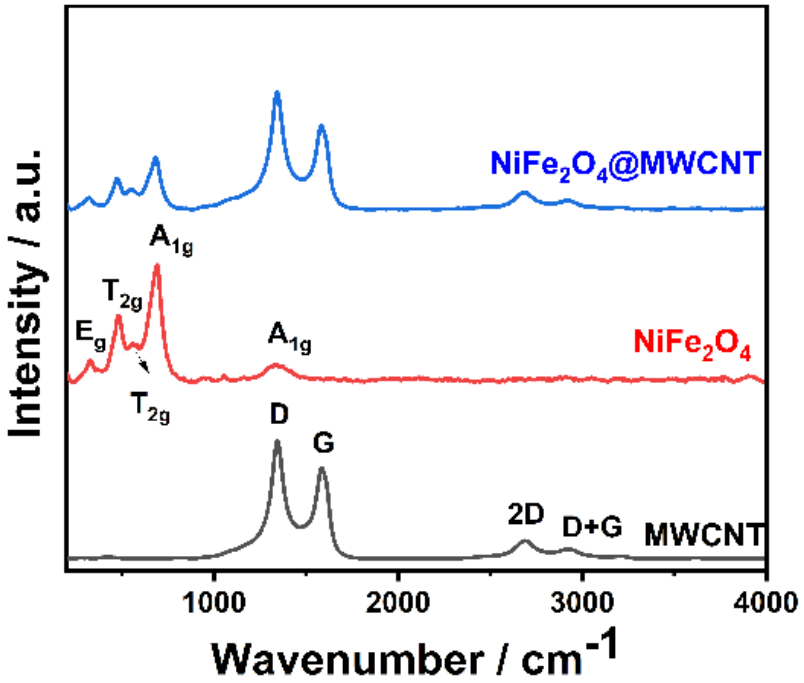

Figure 2. Raman spectra for MWCNT (black line), $NiFe_2O_4$ (red line), and $NiFe_2O_4$@MWCNT (blue line).

3.2. Electrochemical Behavior of $NiFe_2O_4$ and Its Voltammetric Response for GLU

The electrochemical behavior of $NiFe_2O_4$@MWCNT/GCE in an alkaline medium and its potential response to GLU was studied by cyclic voltammetry. Figure 3 exhibits the electrode response for increasing concentrations of GLU, blank experiment (1.0 mol L^{-1} NaOH, pH 14.0) followed by the additions of 2, 6, and 10 mmol L^{-1} GLU. The 1.0 mol L^{-1} NaOH was chosen as the supporting electrolyte because the alkaline medium facilitates the formation of the NiOOH species, which increases the sensitivity of electrochemical sensors for GLU determination, as described elsewhere [58].

It is possible to observe an increase in the current response when the GLU concentration increases, which indicates that the $NiFe_2O_4$@MWCNT composite contributes to the electrocatalytic oxidation of GLU in an alkaline medium. The negligible response was obtained on unmodified GCE or only in the presence of MWCNTs, which confirms the action of $NiFe_2O_4$ within the composite.

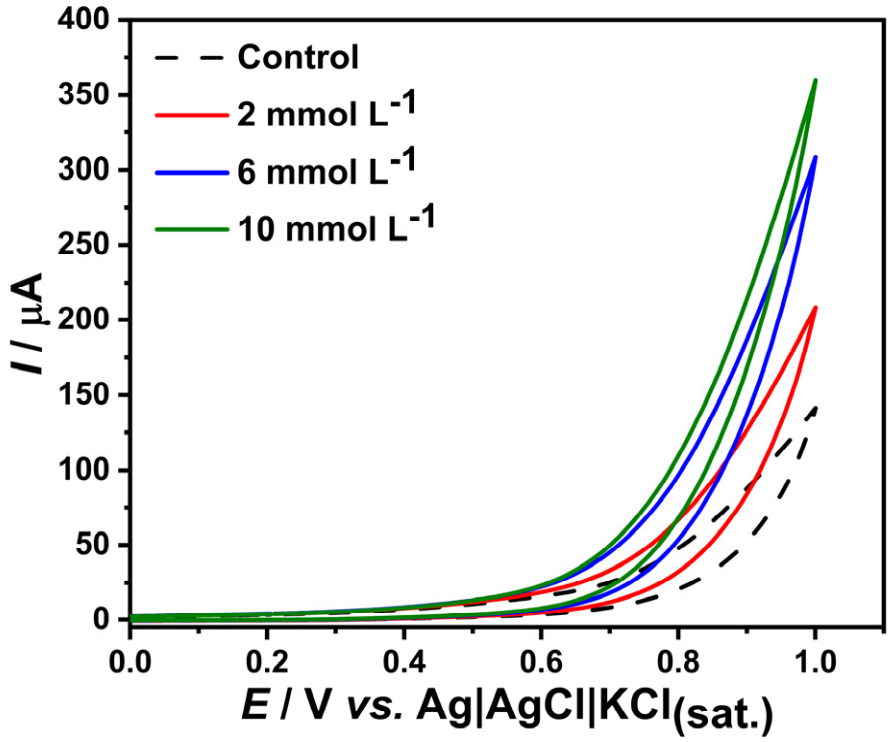

Figure 3. Cyclic voltammograms were obtained on $NiFe_2O_4$@MWCNT/GCE after additions of 2, 6, and 10 mmol L^{-1} GLU. CV conditions: scan rate of 50 mV s^{-1} and step potential of 5 mV. Supporting electrolyte: 1.0 mol L^{-1} NaOH.

The role of $NiFe_2O_4$ on the electrochemical oxidation of GLU can be explained by discussing the mechanism of the electrochemical process of $NiFe_2O_4$ in an alkaline medium, which can be presented as [16,59]:

$$NiFe_2O_4 + H_2O + OH^- \leftrightarrow NiOOH + 2\ FeOOH + e^-$$

The NiOOH species is supposed to be responsible for promoting the electrocatalytic oxidation of GLU [60,61]. In alkaline media, the Ni^{2+} reacts with OH^- radical, forming NiOOH. Subsequently, the NiOOH interacts with hydroxyl groups of GLU, promoting hydrogenation and conversion of GLU to gluconolactone [62], and Ni^{3+}, in turn, is reduced back to Ni^{2+} (Ni^{3+}/Ni^{2+}) as follows [63]:

$$NiOOH + glucose \leftrightarrow Ni(OH)_2 + glucolactone$$

In addition, NiOOH also contributes to water oxidation in an alkaline medium since the formed NiOOH is deprotonated, generating NiO(OH), which is a negatively charged (or proton-deficient) surface species responsible for the increased oxygen evolution activity [54]. Furthermore, the presence of iron may favor the oxygen evolution reaction to occur at lower potentials due to the formation of mixed Ni-Fe oxyhydroxide species [64]. Importantly, no redox signal from Ni^{2+}/Ni^{3+} was observed because the $NiFe_2O_4$ concentration in the composite is low [17,60].

3.3. Amperometric Study of $NiFe_2O_4$@MWCNT/GCE Using BIA-AD System

The performance of $NiFe_2O_4$@MWCNT/GCE for GLU sensing was evaluated using the BIA-AD method to achieve low detection levels of GLU like those found in biological fluids and demonstrate its applicability. The experimental parameters (applied potential, injection volume, and dispensing rate) were systematically evaluated using 100 µmol L^{-1} GLU (n = 3). The study of the applied potential (from +0.5 to +1.0 V) (Figure S3A) shows that

its increasing led to an increase in current. However, despite the highest potential (+1.0 V) showing the highest current, a greater deviation between the injections was observed. For this reason, +0.9 V was chosen for the amperometric detection of GLU since it exhibits a high current and a low deviation between the injections. The other two parameters, injection volume (from 50 to 300 µL) (Figure S3B) and dispensing rate (from 34.5 to 299 µL s^{-1}) (Figure S3C), were also investigated. The chosen injection volume was 250 µL because, in larger volumes, such as 300 µL, there was no considerable increase in current referring to GLU oxidation. At smaller injection volumes, the current signal was lower than the one obtained using 250 µL. The dispensing rate was also evaluated, and 299 µL s^{-1} was the selected condition. This dispensing rate value was chosen because it offered the highest current compared to the other rates evaluated. Figure S3C shows that the low dispensing rate led to a low current for GLU oxidation. This behavior occurs because the current is proportional to the mass transfer provided by the BIA system. Hence, the higher the flow rates (or dispensing rates), the higher the current.

To compare the analytical performance of both $NiFe_2O_4$@MWCNT/GCE and MWCNT /GCE, calibration curves were constructed using GLU concentration levels between 50 to 600 µmol L^{-1} (Figure S4A,B). Slope values of 0.054 and 0.018 µA L µmol^{-1} were found when $NiFe_2O_4$@MWCNT/GCE (red line) and MWCNT/GCE (black line) electrodes were used, respectively (see the respective curves in Figure S4C). Therefore, the presence of $NiFe_2O_4$ in the composite increases the sensitivity (3-fold), showing that $NiFe_2O_4$ acts as a catalyst for GLU oxidation. This increased sensitivity in the presence of $NiFe_2O_4$ is due to the previously discussed mechanism, in which NiOOH mediates the GLU oxidation. The current response observed on MWCNT/GCE was not expected as MWCNTs do not present electrocatalytic action towards GLU oxidation; however, MWCNTs may contain metallic impurities (catalysts used to obtain MWCNTs) that affect the electrochemistry of MWCNT-modified electrodes. The MWCNTs used in this work were previously characterized [65]; although MWCNTs were functionalized using concentrated acid solutions, residual metallic oxides may still be present and can be responsible for the electrocatalytic oxidation of GLU, as shown in Figure S4. Nevertheless, the presence of $NiFe_2O_4$ particles in the composite is essential to promote the highly sensitive detection of GLU.

The precision of the modification process was assessed through inter-electrode studies (n = 4) using 300 µmol L^{-1} GLU (Figure S5A). A relative standard deviation (RSD) value of 10% was found, suggesting that the surface modification with $NiFe_2O_4$@MWCNT/GCE composite is reproducible. Repeatability using the same electrode was also checked with ten consecutive measurements under the same GLU level (300 µmol L^{-1}), as shown in Figure S5B. An RSD value of 2% was found, which confirms the precision of the method. The analytical parameters, such as limit of detection (LOD), correlation coefficients, slope, and intercept obtained for both modified electrodes, are listed in Table 1 [56]. The LOD values were calculated based on the IUPAC definition [66].

Table 1. Analytical parameters were obtained for GLU detection using MWCNT/GCE and $NiFe_2O_4$@MWCNT/GCE coupled to the BIA-AD system.

Analytical Parameters	Electrodes	
	MWCNT/GCE	**$NiFe_2O_4$@MWCNT/GCE**
r^2	0.98	0.99
Sensitivity (µAL µmol^{-1})	0.018 ± 0.001	0.052 ± 0.001
Intercept (µA)	−0.012	2.094
LOD (µmol L^{-1})	84	24

Table 1 shows the improved analytical features obtained by $NiFe_2O_4$@MWCNT/GCE from the amperometric response present in Figure S4C. In addition to the increase in sensitivity (3-fold), a lower LOD was achieved (24 µmol L^{-1}). The literature indicates that the normal GLU levels in the blood range between 8.8 and 10 mmol L^{-1} [67], and when the level of this biomarker increases, its excess is eliminated in urine. In this way, considering

that the GLU concentration in urine is within the $mmol^{-1}$ range, the detectability obtained by the proposed electrode (24 μmol L^{-1}) is feasible to determine GLU in urine samples.

After optimization of the BIA-AD conditions, calibration curves were obtained for GLU concentrations between 50 and 900 μmol L^{-1} in ascending and descending orders using $NiFe_2O_4$@MWCNT/GCE as the working electrode to study the memory effect (Figure 4A). For the ascending curve (Figure 4B, black line), a slope value of 0.051 μAL $μmol^{-1}$ was obtained, while for the descending curve, a slope value of 0.053 μAL $μmol^{-1}$ was achieved (Figure 4B, red line). These results indicate that memory effect and surface fouling were not pronounceable. Moreover, linearity was demonstrated in both cases by the correlation coefficients for ascending curve (r^2 = 0.99) and descending curve (r^2 = 0.98).

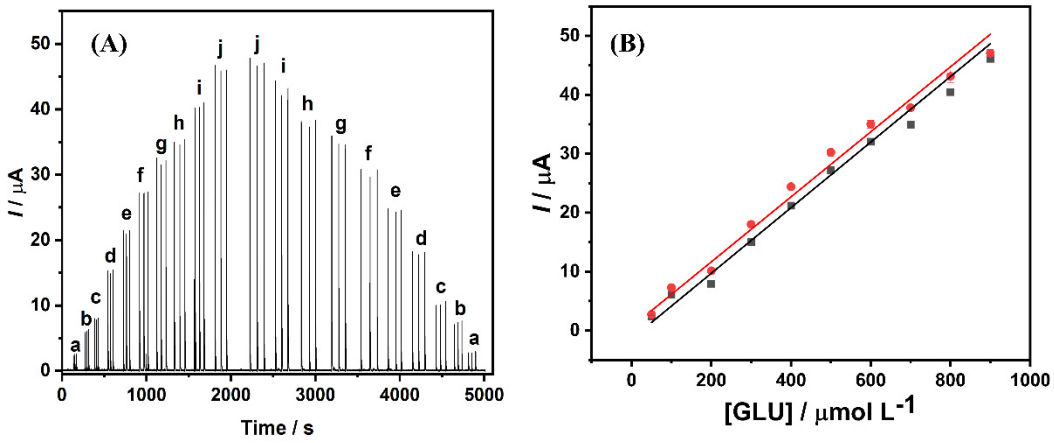

Figure 4. (**A**) BIA amperogram for injections (n = 3) of standard solutions of GLU: (a) 50; (b) 100; (c) 200; (d) 300; (e) 400; (f) 500; (g) 600; (h) 700; (i) 800 and (j) 900 μmol L^{-1} using $NiFe_2O_4$@MWCNT/GCE. (**B**) Calibration curves and respective linear adjustments obtained for ascending (black line) and descending (red line) orders. Supporting electrolyte: 1.0 mol L^{-1} NaOH, potential applied: +0.9 V, injection volume: 250 μL, and dispensing rate: 299 μL s^{-1}.

3.4. Application of $NiFe_2O_4$@MWCNT/GCE for the Determination of GLU in Synthetic Urine Using the BIA-AD System

The $NiFe_2O_4$@MWCNT/GCE was applied for GLU determination in synthetic urine (200-fold diluted) spiked with GLU at two concentration levels (100 and 300 μmol L^{-1}). The urine sample was diluted to reduce the sample matrix effect on the detection of GLU. Figure 5 shows a calibration curve obtained with triplicate injections of standard solutions of GLU followed by triplicate injections of the non-spiked and spiked urine samples. It is possible to observe that the sample presented a small signal that was below the first standard concentration value, so this analytical signal cannot be used to quantify GLU in the sample. Since no GLU was added to the synthetic sample, this signal can be a result of the sample matrix. Considering the spiked samples, acceptable recovery values were obtained, 84% and 95% for urine spiked with 100 and 300 μmol L^{-1} GLU, respectively [68]. Based on this, the method presented satisfactory accuracy for the urine sample analysis. Table 2 shows the results of the analysis of spiked synthetic urine using two concentrations levels of GLU (100 and 300 μmol L^{-1}).

Since uric acid (UA), ascorbic acid (AA), and urea (U) are biomarkers commonly found in urine samples [69], the influence of these species on GLU quantification was properly evaluated. Moreover, the influence of inorganic salts (NaCl, $NaHCO_3$, and $CaCl_2$) present in urine samples was also verified. Figure 6 shows the response variation of 1.0 mmol L^{-1} GLU in the presence of 0.1 mmol L^{-1} UA, AA, U, NaCl, $NaHCO_3$, and $CaCl_2$. This experiment was evaluated under BIA-AD optimized conditions (conditions of Figure 4). The concentrations of GLU and interferents were selected considering the typical composition of urine samples [61].

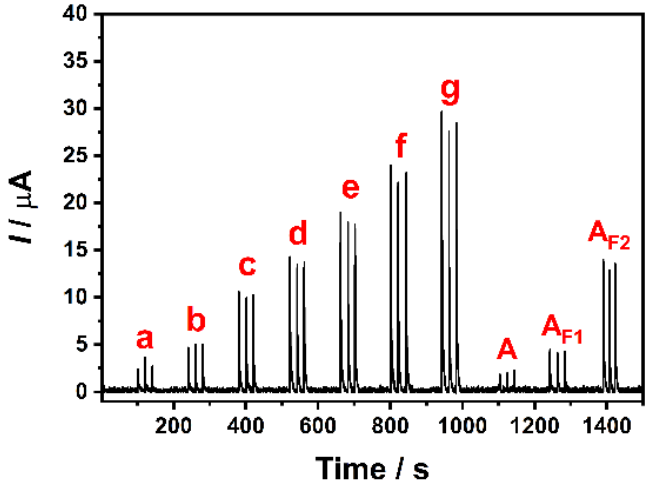

Figure 5. BIA amperogram for the analysis of urine obtained for triplicate injections of standard solutions of GLU: (a) 50; (b) 100; (c) 200; (d) 300; (e) 400; (f) 500; and (g) 600 μmol L^{-1}; followed by triplicate injections of sample solutions: (A) non-spiked and spiked urine samples (A_{F1}) with 100 μmol L^{-1} and (A_{F2}) with 300 μmol L^{-1}. Supporting electrolyte: 1.0 mol L^{-1} NaOH, potential applied: +0.9 V, injection volume: 250 μL, and dispensing rate: 299 μL s^{-1}.

Table 2. GLU concentrations and recovery values were obtained for the analysis of spiked synthetic urine.

Sample	Spiked/μmol L^{-1}	Found/μmol L^{-1}	Recovery/%
Synthetic urine	100	83.9	83.9
	300	284.2	94.7

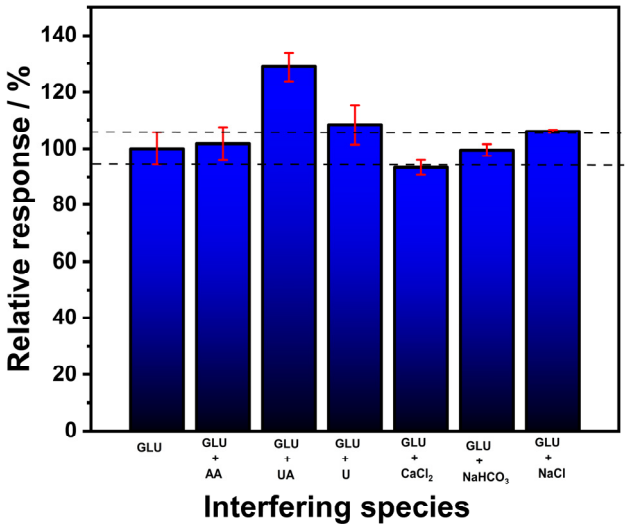

Figure 6. Amperometric response variation (n = 3) of 1 mmol L^{-1} GLU in the presence of possible interfering species (AA, UA, U, $CaCl_2$, $NaHCO_3$, and NaCl) at 0.1 mmol L^{-1}. Data obtained from BIA-AD measurements under optimized conditions. The dashed lines represent the acceptable range of variation in the relative response (± 5 %).

It is possible to observe that only UA presented significant interference (around +28%); therefore, a detailed individual study was carried out for this interference. Figure S6 shows the impact of UA at different concentrations (from 0.05 to 0.1 mmol L^{-1}) on the electrochemical response of 1 mmol L^{-1} GLU. Using 0.08 mmol L^{-1} of UA, there was no significant interference (variation lower than 3%). Under these conditions, $NiFe_2O_4$@MWCNT/GCE can be used to detect GLU in urine samples due to its selectivity and sensitivity. In the presence of high levels of UA, an interesting alternative would be to incorporate a Nafion

membrane on the surface of our sensor, which has proven to be effective in eliminating UA interference on the electrochemical response of GLU [70].

The analytical performance of $NiFe_2O_4$/MWCNT/GCE based on LOD and linear range was compared with other non-enzymatic sensors reported in the literature for GLU sensing (Table 3). It can be highlighted that the proposed sensor showed improved performance, attested by the wider working range and better detectability. Importantly, the sensor was precise, accurate, and successfully coupled to the high-throughput BIA system (77 injections can be performed in one hour), thus confirming that the combination of $NiFe_2O_4$/MWCNT/GCE with BIA-AD is a valuable strategy for routine clinical analysis.

Table 3. Performance of $NiFe_2O_4$/MWCNT/GCE compared with other non-enzymatic electrodes.

Material	LOD (μmol L^{-1})	Linear Range (mmol L^{-1})	Sample	Type of Sensor	Ref.
$CoFe_2O_4$/Nickel foil	100	0.1–1.1	Blood	Non-enzymatic	[71]
CuO/NiO-C/CT	37	0.1–2.5	Human serum samples	Non-enzymatic	[72]
$ZnFe_2O_4$/ppy	100	0.1–8.0	Human serum samples	Non-enzymatic	[73]
$Ni(OH)_2$/AuNP/SPE	40	0.1–2.0	Artificial saliva samples	Non-enzymatic	[11]
CHIT/$NiFe_2O_4$/GCE	-	0.1–20.0	-	Enzymatic	[7]
GOx-AC-$NiFe_2O_4$/CPE	1100.0	2.0–10.0	Blood sample	Enzymatic	[6]
$NiFe_2O_4$/CNTs	2.2	0.005–0.06	Juice samples	Enzymatic	[5]
$NiFe_2O_4$/CNTs	98.0	0.0–3.0 and 3.2–12.4	-	Enzymatic	[74]
$NiFe_2O_4$@MWCNT/GCE	24	0.05–0.6	Artificial urine	Non-enzymatic	This work

CuO/NiO-C: Metal oxide-carbon composite; **CT**: cello tape; ppy: polypyrrole; **AuNP**: gold nanoparticles; **CHIT**: chitosan; **GOx**: glucose oxidase; **CPE**: carbon paste electrode; **CNTs**: carbon nanotubes; **SPE**: screen-printed electrodes; **MWCNT**: multi-walled nanotubes; **GCE**: glassy-carbon electrode.

4. Conclusions

It was demonstrated that the composite formed by $NiFe_2O_4$ and MWCNT is a potential material for developing non-enzymatic sensors for GLU. The synthesis of $NiFe_2O_4$ by coprecipitation with hydrothermal treatment provided particles with high crystallinity and no impurities. Detailed electrochemical studies using the $NiFe_2O_4$@MWCNT/GCE showed the importance of the presence of $NiFe_2O_4$, which catalyzed the oxidation of GLU and consequently improved the sensitivity for GLU sensing. It is important to note that the proposed device provided suitable detectability for monitoring GLU levels in biological fluids. Moreover, the sensor fabrication procedure is reproducible, considering the reproducibility study for four different electrodes (RSD = 10%). When associated with the BIA-AD system, it enabled satisfactory analysis of synthetic urine samples (recoveries above 83.9%). In addition, the proposed sensor is free from interference of other biomarker species present in urine. Therefore, it can be considered a useful alternative platform for clinical studies aimed at monitoring GLU in biological fluids.

Supplementary Materials: The following supporting information can be downloaded at: https://www.mdpi.com/article/10.3390/chemosensors12060112/s1, Figure S1: SEM images of (A) $NiFe_2O_4$@MWCNT composite and (B) functionalized MWCNT; Figure S2: EDS spectrum of $NiFe_2O_4$ (A); MWCNT (B) and $NiFe_2O_4$@MWCNT composite (C). Figure S3: Impact of the BIA-AD parameters (A) applied potential, (B) injection volume, and (C) dispensing rate on the electrochemical response of 100 μmol L^{-1} GLU. Figure S4: Amperometric response using BIA-AD system for GLU injections (n = 3) with concentrations of (a) 50; (b) 100; (c) 200; (d) 300; (e) 400; (f) 500 and (g) 600 μmol L^{-1} on the (A) MWCNT/GCE and (B) $NiFe_2O_4$@MWCNT/GCE electrodes. (C) Calibration curves obtained from 50 to 600 μmol L^{-1} GLU using $NiFe_2O_4$@MWCNT/GCE (red line) and MWCNT/GCE (black line). Supporting electrolyte: 1.0 mol L^{-1} NaOH, applied potential: + 0.9 V, injection volume: 250 μL and dispensing rate: 299 μL s^{-1}. Figure S5: (A) Reproducibility study (inter-electrodes, n = 4) using 300 μmol L^{-1} GLU with $NiFe_2O_4$@MWCNT/GCE coupled to the BIA-AD system. (B) Repeatability study (intra-electrodes, n = 10) using 300 μmol L^{-1} GLU with $NiFe_2O_4$@MWCNT/GCE coupled to the BIA-AD system. Figure S6: Relative amperometric response for GLU (1.00 mmol L^{-1}) before (first bar named as GLU) and after the addition of UA at different concentrations (from 1.00 to 0.05 mmol L^{-1}).

Author Contributions: Conceptualization, A.B.N., R.A.A.M., and O.F.L.; methodology, A.B.N., R.A.A.M., O.F.L., L.V.d.F., and T.A.M.; data curation, A.B.N., L.V.d.F., and T.A.M.; draft writing, A.B.N., writing and review, A.B.N., R.A.A.M., O.F.L., L.V.d.F., and T.A.M. All authors have read and agreed to the published version of the manuscript.

Funding: This research was funded by FAPEMIG (APQ-02391-22 and APQ-00282-21), CNPq (315838/2021-3; 1633330/2020-4; 151006/2022-9; 382326/2022-9; 302839/2020-8; and 406026/2023-8), CAPES (financial code 001) and INCTBio (CNPq/INCT 465389/2014-7).

Institutional Review Board Statement: Not applicable.

Informed Consent Statement: Not applicable.

Data Availability Statement: The original contributions presented in the study are included in the article/Supplementary Material, further inquiries can be directed to the corresponding author/s.

Acknowledgments: The authors are grateful to the Brazilian agencies FAPEMIG (APQ-02391-22 and APQ-00282-21), CNPq (315838/2021-3; 1633330/2020-4; 151006/2022-9; 382326/2022-9; 302839/2020-8; and 406026/2023-8), CAPES (financial code 001) and INCTBio (CNPq/INCT 465389/2014-7). We are also grateful to the multiuser laboratory of the Institute of Physics (INFIS) supported by CAPES and to the university Multiuser laboratory (RELAM-UFU) for the SEM experiments.

Conflicts of Interest: The authors declare no conflicts of interest.

References

1. Hasanzadeh, M.; Sayadi, M.; Alizadeh, S.; Ghasemlu, K. Modification of Multi-Walled Carbon Nanotubes Composite Paste Electrode with Nanonickel Pentacyanonitrosylferrate and Nickel Oxide Nanoparticles for Non-Enzymatic Glucose Determination. *Iran. Chem. Soc. Anal. Bioanal. Chem. Res.* **2023**, *10*, 183–192.
2. Morikawa, M.-A.; Kimizuka, N.; Yoshihara, M.; Endo, T. New Colorimetric Detection of Glucose by Means of Electron-Accepting Indicators: Ligand Substitution of $[Fe(Acac)_{3-n}(Phen)_n]^{n+}$ Complexes Triggered by Electron Transfer from Glucose Oxidase. *Chem. A Eur. J.* **2002**, *8*, 5580–5584. [CrossRef]
3. Wei, Y.; Hui, Y.; Lu, X.; Liu, C.; Zhang, Y.; Fan, Y.; Chen, W. One-Pot Preparation of NiMn Layered Double Hydroxide-MOF Material for Highly Sensitive Electrochemical Sensing of Glucose. *J. Electroanal. Chem.* **2023**, *933*, 117276. [CrossRef]
4. Wang, G.; He, X.; Wang, L.; Gu, A.; Huang, Y.; Fang, B.; Geng, B.; Zhang, X. Non-Enzymatic Electrochemical Sensing of Glucose. *Microchim. Acta* **2013**, *180*, 161–186. [CrossRef]
5. Wu, L.; Zhou, X.; Wan, G.; Shi, S.; Wang, G. $NiFe_2O_4$/CNTs Fabricated by Atomic Layer Deposition as Highly Stable Peroxidase Mimics for Sensitive Colorimetric Detection of Hydrogen Peroxide and Glucose. *Mater. Res. Bull.* **2022**, *147*, 111637. [CrossRef]
6. Fatoni, A.; Widanarto, W.; Anggraeni, M.D.; Dwiasi, D.W. Glucose Biosensor Based on Activated Carbon—$NiFe_2O_4$ Nanoparticles Composite Modified Carbon Paste Electrode. *Results Chem.* **2022**, *4*, 100433. [CrossRef]
7. Luo, L.; Li, Q.; Xu, Y.; Ding, Y.; Wang, X.; Deng, D.; Xu, Y. Amperometric Glucose Biosensor Based on $NiFe_2O_4$ Nanoparticles and Chitosan. *Sens. Actuators B Chem.* **2010**, *145*, 293–298. [CrossRef]
8. Ramesh, M.; Sankar, C.; Umamatheswari, S.; Balamurugan, J.; Jayavel, R.; Gowran, M. Hydrothermal Synthesis of $ZnZrO_2$/Chitosan ($ZnZrO_2$/CS) Nanocomposite for Highly Sensitive Detection of Glucose and Hydrogen Peroxide. *Int. J. Biol. Macromol.* **2023**, *226*, 618–627. [CrossRef] [PubMed]
9. Muqaddas, S.; Javed, M.; Nadeem, S.; Asghar, M.A.; Haider, A.; Ahmad, M.; Ashraf, A.R.; Nazir, A.; Iqbal, M.; Alwadai, N.; et al. Carbon Nanotube Fiber-Based Flexible Microelectrode for Electrochemical Glucose Sensors. *ACS Omega* **2022**, *8*, 2272–2280. [CrossRef]
10. Yang, S.; Li, G.; Wang, D.; Qiao, Z.; Qu, L. Synthesis of Nanoneedle-like Copper Oxide on N-Doped Reduced Graphene Oxide: A Three-Dimensional Hybrid for Nonenzymatic Glucose Sensor. *Sens. Actuators B Chem.* **2017**, *238*, 588–595. [CrossRef]
11. Rinaldi, A.L.; Rodríguez-Castellón, E.; Sobral, S.; Carballo, R. Application of a Nickel Hydroxide Gold Nanoparticles Screen-Printed Electrode for Impedimetric Sensing of Glucose in Artificial Saliva. *J. Electroanal. Chem.* **2019**, *832*, 209–216. [CrossRef]
12. Tee, S.Y.; Teng, C.P.; Ye, E. Metal Nanostructures for Non-Enzymatic Glucose Sensing. *Mater. Sci. Eng. C* **2017**, *70*, 1018–1030. [CrossRef] [PubMed]
13. Ataei Kachouei, M.; Shahrokhian, S.; Ezzati, M. Bimetallic CoZn-MOFs Easily Derived from CoZn-LDHs, as a Suitable Platform in Fabrication of a Non-Enzymatic Electrochemical Sensor for Detecting Glucose in Human Fluids. *Sens. Actuators B Chem.* **2021**, *344*, 130254. [CrossRef]
14. Gonçalves, J.M.; Rocha, D.P.; Silva, M.N.T.; Martins, P.R.; Nossol, E.; Angnes, L.; Rout, C.S.; Munoz, R.A.A. Feasible Strategies to Promote the Sensing Performances of Spinel MCo_2O_4 (M = Ni, Fe, Mn, Cu and Zn) Based Electrochemical Sensors: A Review. *J. Mater. Chem. C Mater.* **2021**, *9*, 7852–7887. [CrossRef]
15. Naik, K.K.; Sahoo, S.; Rout, C.S. Facile Electrochemical Growth of Spinel Copper Cobaltite Nanosheets for Non-Enzymatic Glucose Sensing and Supercapacitor Applications. *Microporous Mesoporous Mater.* **2017**, *244*, 226–234. [CrossRef]

16. Franceschini, F.; Taurino, I. Nickel-Based Catalysts for Non-Enzymatic Electrochemical Sensing of Glucose: A Review. *Phys. Med.* **2022**, *14*, 100054. [CrossRef]
17. Danaee, I.; Jafarian, M.; Forouzandeh, F.; Gobal, F. Kinetic Studies of Glucose Electrocatalytic Oxidation on GC/Ni Electrode. *Int. J. Chem. Kinet.* **2012**, *44*, 712–721. [CrossRef]
18. Chen, C.; Xie, Q.; Yang, D.; Xiao, H.; Fu, Y.; Tan, Y.; Yao, S. Recent Advances in Electrochemical Glucose Biosensors: A Review. *RSC Adv.* **2013**, *3*, 4473. [CrossRef]
19. Gonçalves, J.M.; de Faria, L.V.; Nascimento, A.B.; Germscheidt, R.L.; Patra, S.; Hernández-Saravia, L.P.; Bonacin, J.A.; Munoz, R.A.A.; Angnes, L. Sensing Performances of Spinel Ferrites MFe_2O_4 (M = Mg, Ni, Co, Mn, Cu and Zn) Based Electrochemical Sensors: A Review. *Anal. Chim. Acta* **2022**, *1233*, 340362. [CrossRef]
20. Chu, D.; Li, F.; Song, X.; Ma, H.; Tan, L.; Pang, H.; Wang, X.; Guo, D.; Xiao, B. A Novel Dual-Tasking Hollow Cube $NiFe_2O_4$-NiCo-LDH@rGO Hierarchical Material for High Preformance Supercapacitor and Glucose Sensor. *J. Colloid. Interface Sci.* **2020**, *568*, 130–138. [CrossRef]
21. Bashal, A.H.; Hefnawy, M.A.; Ahmed, H.A.; El-Atawy, M.A.; Pashameah, R.A.; Medany, S.S. Green Synthesis of $NiFe_2O_4$ Nano-Spinel Oxide-Decorated Carbon Nanotubes for Efficient Capacitive Performance—Effect of Electrolyte Concentration. *Nanomaterials* **2023**, *13*, 2643. [CrossRef] [PubMed]
22. Afkhami, A.; Khoshsafar, H.; Bagheri, H.; Madrakian, T. Preparation of $NiFe_2O_4$/Graphene Nanocomposite and Its Application as a Modifier for the Fabrication of an Electrochemical Sensor for the Simultaneous Determination of Tramadol and Acetaminophen. *Anal. Chim. Acta* **2014**, *831*, 50–59. [CrossRef]
23. Katowah, D.F.; Hussein, M.A.; Alam, M.M.; Ismail, S.H.; Osman, O.I.; Sobahi, T.R.; Asiri, A.M.; Ahmed, J.; Rahman, M.M. Designed Network of Ternary Core-Shell PPCOT/NiFe2O4/C-SWCNTs Nanocomposites. A Selective Fe^{3+} Ionic Sensor. *J. Alloys Compd.* **2020**, *834*, 155020. [CrossRef]
24. Hosseinpour, A.; Sadeghi, H.; Morisako, A. Simulation of DC-Hopping Conduction in Spinel Ferrites Using Free Electron Gas Model. *J. Magn. Magn. Mater.* **2007**, *316*, e283–e286. [CrossRef]
25. Schroeder, V.; Savagatrup, S.; He, M.; Lin, S.; Swager, T.M. Carbon Nanotube Chemical Sensors. *Chem. Rev.* **2019**, *119*, 599–663. [CrossRef] [PubMed]
26. Mehmandoust, M.; Pourhakkak, P.; Tiris, G.; Karimi-Maleh, H.; Erk, N. A Reusable and Sensitive Electrochemical Sensor for Determination of Idarubicin in Environmental and Biological Samples Based on $NiFe_2O_4$ Nanospheres Anchored N-Doped Graphene Quantum Dots Composite; an Electrochemical and Molecular Docking Investigation. *Environ. Res.* **2022**, *212*, 113264. [CrossRef] [PubMed]
27. Askari, N.; Salarizadeh, N.; Askari, M.B. Electrochemical Determination of Rutin by Using $NiFe_2O_4$ Nanoparticles-Loaded Reduced Graphene Oxide. *J. Mater. Sci. Mater. Electron.* **2021**, *32*, 9765–9775. [CrossRef] [PubMed]
28. Ensafi, A.A.; Jafari-Asl, M.; Rezaei, B.; Allafchian, A.R. Simultaneous Determination of Guanine and Adenine in DNA Based on $NiFe_2O_4$ Magnetic Nanoparticles Decorated MWCNTs as a Novel Electrochemical Sensor Using Adsorptive Stripping Voltammetry. *Sens. Actuators B Chem.* **2013**, *177*, 634–642. [CrossRef]
29. Kuznowicz, M.; Rębiś, T.; Jędrzak, A.; Nowaczyk, G.; Szybowicz, M.; Jesionowski, T. Glucose Determination Using Amperometric Non-Enzymatic Sensor Based on Electroactive Poly(Caffeic Acid)@MWCNT Decorated with CuO Nanoparticles. *Microchim. Acta* **2022**, *189*, 159. [CrossRef]
30. Rocha, D.P.; Cardoso, R.M.; Tormin, T.F.; de Araujo, W.R.; Munoz, R.A.A.; Richter, E.M.; Angnes, L. Batch-injection Analysis Better than Ever: New Materials for Improved Electrochemical Detection and On-site Applications. *Electroanalysis* **2018**, *30*, 1386–1399. [CrossRef]
31. Haššo, M.; Švorc, Ľ. Batch Injection Analysis in Tandem with Electrochemical Detection: The Recent Trends and an Overview of the Latest Applications (2015–2020). *Monatshefte Chem.-Chem. Mon.* **2022**, *153*, 985–1000. [CrossRef] [PubMed]
32. Garcia, P.T.; Dias, A.A.; Souza, J.A.C.; Coltro, W.K.T. Batch Injection Analysis towards Auxiliary Diagnosis of Periodontal Diseases Based on Indirect Amperometric Detection of Salivary α-Amylase on a Cupric Oxide Electrode. *Anal. Chim. Acta* **2018**, *1041*, 50–57. [CrossRef] [PubMed]
33. Veloso, W.B.; Ribeiro, G.A.C.; da Rocha, C.Q.; Tanaka, A.A.; da Silva, I.S.; Dantas, L.M.F. Flow-through Amperometric Determination of Ampicillin Using a Copper Electrode in a Batch Injection Analysis System. *Measurement* **2020**, *155*, 107516. [CrossRef]
34. Quintino, M.S.M.; Angnes, L. Batch Injection Analysis: An Almost Unexplored Powerful Tool. *Electroanalysis* **2004**, *16*, 513–523. [CrossRef]
35. Brooks, T.; Keevil, C.W. A Simple Artificial Urine for the Growth of Urinary Pathogens. *Lett. Appl. Microbiol.* **1997**, *24*, 203–206. [CrossRef] [PubMed]
36. Kurian, J.; Lahiri, B.B.; Mathew, M.J.; Philip, J. High Magnetic Fluid Hyperthermia Efficiency in Copper Ferrite Nanoparticles Prepared by Solvothermal and Hydrothermal Methods. *J. Magn. Magn. Mater.* **2021**, *538*, 168223. [CrossRef]
37. de Matos Morawski, F.; Caon, N.B.; Sousa, K.A.P.; Faita, F.L.; Parize, A.L.; Jost, C.L. Hybrid Chitosan-Coated Manganese Ferrite Nanoparticles for Electrochemical Sensing of Bifenox Herbicide. *J. Environ. Chem. Eng.* **2021**, *9*, 106298. [CrossRef]
38. Adibi, M.; Mirkazemi, S.M.; Alamolhoda, S. The Influence of Citric Acid on the Microstructure and Magnetic Properties of Cobalt Ferrite Nanoparticles Synthesized by Hydrothermal Method. *Appl. Phys. A Mater. Sci. Process* **2021**, *127*, 497. [CrossRef]

39. Xian, G.; Kong, S.; Li, Q.; Zhang, G.; Zhou, N.; Du, H.; Niu, L. Synthesis of Spinel Ferrite MFe_2O_4 (M = Co, Cu, Mn, and Zn) for Persulfate Activation to Remove Aqueous Organics: Effects of M-Site Metal and Synthetic Method. *Front. Chem.* **2020**, *8*, 177. [CrossRef]
40. Cao, Z.; Qiu, L.; Yang, Y.; Chen, Y.; Liu, X. The Surface Modifications of Multi-Walled Carbon Nanotubes for Multi-Walled Carbon Nanotube/Poly(Ether Ether Ketone) Composites. *Appl. Surf. Sci.* **2015**, *353*, 873–881. [CrossRef]
41. Lu, C.; Lin, F.; Shao, H.; Bi, S.; Chen, N.; Shao, G.; Jiang, J. Carboxylated Carbon Nanotube/Polyimide Films with Low Thermal Expansion Coefficient and Excellent Mechanical Properties. *Polymers* **2022**, *14*, 4565. [CrossRef] [PubMed]
42. Ferrer, C.; Isasi, J.; Arévalo, P.; Fernández-Ramos, M.; Rapp, M.; Alcolea, M.; Marco, J.F.; Martín-Hernández, F. Structural and Magnetic Studies of $NiFe_2O_4$ and $NiFe_2O_4$@SiO_2-Silane Agent Samples Useful for the Removal of Cu^{2+} Ions. *J. Alloys Compd.* **2022**, *899*, 163403. [CrossRef]
43. Wang, W.; Ding, Z.; Zhao, X.; Wu, S.; Li, F.; Yue, M.; Liu, J.P. Microstructure and Magnetic Properties of MFe_2O_4 (M = Co, Ni, and Mn) Ferrite Nanocrystals Prepared Using Colloid Mill and Hydrothermal Method. *J. Appl. Phys.* **2015**, *117*, 17A328. [CrossRef]
44. Soto-Arreola, A.; Huerta-Flores, A.M.; Mora-Hernández, J.M.; Torres-Martínez, L.M. Comparative Study of the Photocatalytic Activity for Hydrogen Evolution of MFe_2O_4 (M = Cu, Ni) Prepared by Three Different Methods. *J. Photochem. Photobiol. A Chem.* **2018**, *357*, 20–29. [CrossRef]
45. Sankaranarayanan, R.; Shailajha, S.; Mubina, M.S.K.; Anilkumar, C.P. Effect of Ni^{2+} and Fe^{3+} Ion Concentrations on Structural, Optical, Magnetic, and Impedance Response of NiFe2O4 Nanoparticles Prepared by Sol-Gel Process. *J. Supercond. Nov. Magn.* **2020**, *33*, 3631–3642. [CrossRef]
46. Ayyappan, S.; Mahadevan, S.; Chandramohan, P.; Srinivasan, M.P.; Philip, J.; Raj, B. Influence of Co^{2+} Ion Concentration on the Size, Magnetic Properties, and Purity of $CoFe_2O_4$ Spinel Ferrite Nanoparticles. *J. Phys. Chem. C* **2010**, *114*, 6334–6341. [CrossRef]
47. Esther Nimshi, R.; Judith Vijaya, J.; Al-Najar, B.; Hazeem, L.; Bououdina, M.; John Kennedy, L.; Kombaiah, K.; Bellucci, S. Multifunctional Core-Shell NiFe2O4Shield with TiO_2/RGO Nanostructures for Biomedical and Environmental Applications. *Bioinorg. Chem. Appl.* **2022**, *2022*, 4805490. [CrossRef] [PubMed]
48. Wei, Z.; Li, H.; Wu, J.; Dong, Y.; Zhang, H.; Chen, H.; Ren, C. 3DRGO-$NiFe_2O_4$/NiO Nanoparticles for Fast and Simple Detection of Organophosphorus Pesticides. *Chin. Chem. Lett.* **2020**, *31*, 177–180. [CrossRef]
49. Zeshan, M.; Waheed, M.S.; Ishaq, S.A.; Siddique, A.; Ullah, A.; Sherif, E.S.M.; Ansari, M.Z.; Khan, S.A.; Khan, A.R.; Farid, H.M.T. Sol–Gel Preparation of Spinel Ferrites/Polyaniline Composites for Electromagnetic Interface Shielding. *Chem. Pap.* **2023**, *77*, 6533–6542. [CrossRef]
50. Larrude, D.G.; Maia Da Costa, M.E.H.; Freire, F.L. Synthesis and Characterization of Silver Nanoparticle-Multiwalled Carbon Nanotube Composites. *J. Nanomater.* **2014**, *2014*, 654068. [CrossRef]
51. Prajapati, N.; Murthy, C.N.; Machhi, H.K.; Soni, S.S. A Novel F-MWCNT-Based Nanocomposite for Enhancement of Photoconversion Efficiency of DSSC. *J. Mater. Sci. Mater. Electron.* **2023**, *34*, 2129. [CrossRef]
52. Ma, W.; Zhao, Y.; Zhu, Z.; Guo, L.; Cao, Z.; Xia, Y.; Yang, H.; Gong, F.; Zhong, J. Synthesis of Poly(Methyl Methacrylate) Grafted Multiwalled Carbon Nanotubes via a Combination of RAFT and Alkyne-Azide Click Reaction. *Appl. Sci.* **2019**, *9*, 603. [CrossRef]
53. Feng, J.M.; Dai, Y.J. Water-Assisted Growth of Graphene on Carbon Nanotubes by the Chemical Vapor Deposition Method. *Nanoscale* **2013**, *5*, 4422–4426. [CrossRef] [PubMed]
54. Ferrari, A.C.; Meyer, J.C.; Scardaci, V.; Casiraghi, C.; Lazzeri, M.; Mauri, F.; Piscanec, S.; Jiang, D.; Novoselov, K.S.; Roth, S.; et al. Raman Spectrum of Graphene and Graphene Layers. *Phys. Rev. Lett.* **2006**, *97*, 187401. [CrossRef] [PubMed]
55. Chandramohan, P.; Srinivasan, M.P.; Velmurugan, S.; Narasimhan, S.V. Cation Distribution and Particle Size Effect on Raman Spectrum of $CoFe_2O_4$. *J. Solid. State Chem.* **2011**, *184*, 89–96. [CrossRef]
56. Ortiz-Quiñonez, J.L.; Pal, U.; Villanueva, M.S. Structural, Magnetic, and Catalytic Evaluation of Spinel Co, Ni, and Co-Ni Ferrite Nanoparticles Fabricated by Low-Temperature Solution Combustion Process. *ACS Omega* **2018**, *3*, 14986–15001. [CrossRef]
57. Sahoo, P.; Shrestha, R.G.; Shrestha, L.K.; Hill, J.P.; Takei, T.; Ariga, K. Surface Oxidized Carbon Nanotubes Uniformly Coated with Nickel Ferrite Nanoparticles. *J. Inorg. Organomet. Polym. Mater.* **2016**, *26*, 1301–1308. [CrossRef]
58. Wang, S.; Zhang, L.; Tian, Y.; Lin, L.; Zhuiykov, S. Fabrication of $Ni(OH)_2$&NiOOH Film/Ni Electrode and the Effect of NaOH Concentration on Its Glucose Detection. *J. Electrochem. Soc.* **2019**, *166*, B1732–B1741. [CrossRef]
59. Zhang, X.; Zhang, Z.; Sun, S.; Wu, Y.; Sun, Q.; Liu, X. A Facile One-Step Hydrothermal Approach to Synthesize Hierarchical Core-Shell $NiFe_2O_4$@$NiFe_2O_4$ Nanosheet Arrays on Ni Foam with Large Specific Capacitance for Supercapacitors. *RSC Adv.* **2018**, *8*, 15222–15228. [CrossRef]
60. Trafela, Š.; Zavašnik, J.; Šturm, S.; Rožman, K.Ž. Formation of a $Ni(OH)_2$/NiOOH Active Redox Couple on Nickel Nanowires for Formaldehyde Detection in Alkaline Media. *Electrochim. Acta* **2019**, *309*, 346–353. [CrossRef]
61. Rocha, R.G.; Cardoso, R.M.; Zambiazi, P.J.; Castro, S.V.F.; Ferraz, T.V.B.; Aparecido, G.d.O.; Bonacin, J.A.; Munoz, R.A.A.; Richter, E.M. Production of 3D-Printed Disposable Electrochemical Sensors for Glucose Detection Using a Conductive Filament Modified with Nickel Microparticles. *Anal. Chim. Acta* **2020**, *1132*, 1–9. [CrossRef]
62. Silva, M.N.T.; Rocha, R.G.; Richter, E.M.; Munoz, R.A.A.; Nossol, E. Nickel Oxy-Hydroxy/Multi-Wall Carbon Nanotubes Film Coupled with a 3D-Printed Device as a Nonenzymatic Glucose Sensor. *Biosensors* **2023**, *13*, 646. [CrossRef]
63. Akbar, F.; Tariq, M.; Khan, H.U.; Khan, J.; Uddin, M.K.; Ahmed, S.S.; Rahim, A. Development of Ag–Ni NPs Loaded on MWCNTs for Highly Sensitive, Selective and Reproducible Non-Enzymatic Electrochemical Detection of Glucose. *J. Mater. Sci. Mater. Electron.* **2021**, *32*, 16166–16181. [CrossRef]

64. Diaz-Morales, O.; Ferrus-Suspedra, D.; Koper, M.T.M. The Importance of Nickel Oxyhydroxide Deprotonation on Its Activity towards Electrochemical Water Oxidation. *Chem. Sci.* **2016**, *7*, 2639–2645. [CrossRef]
65. Stefano, J.S.; Lima, A.P.; Nascentes, C.C.; Krzyzaniak, S.R.; Mello, P.A.; Gonçalves, J.M.; Richter, E.M.; Nossol, E.; Munoz, R.A.A. Electrochemical Detection of 2,4,6-Trinitrotoluene on Carbon Nanotube Modified Electrode: Effect of Acid Functionalization. *J. Solid State Electrochem.* **2020**, *24*, 121–129. [CrossRef]
66. Mocak, J.; Bonda, A.M.; Mitchella, S.; Scollaryb, G. A Statistical Overview of Standard (IUPAC and ACS) and New Procedures for Determining the Limits of Detection and Quantification: Application to Voltammetric and Stripping Techniques. *Pure Appl. Chem.* **1997**, *69*, 297–328. [CrossRef]
67. Wang, T.-T.; Huang, X.-F.; Huang, H.; Luo, P.; Qing, L.-S. Nanomaterial-Based Optical- and Electrochemical-Biosensors for Urine Glucose Detection: A Comprehensive Review. *Adv. Sens. Energy Mater.* **2022**, *1*, 100016. [CrossRef]
68. Latimer, G.W., Jr. *Guidelines for Standard Method Performance Requirements: Official Methods of Analysis*; AOAC International: Rockville, MD, USA, 2016.
69. Zhou, F.; Jing, W.; Liu, S.; Mao, Q.; Xu, Y.; Han, F.; Wei, Z.; Jiang, Z. Electrodeposition of Gold Nanoparticles on ZnO Nanorods for Improved Performance of Enzymatic Glucose Sensors. *Mater. Sci. Semicond. Process* **2020**, *105*, 104708. [CrossRef]
70. Yuan, C.-J.; Hsu, C.-L.; Wang, S.-C.; Chang, K.-S. Eliminating the Interference of Ascorbic Acid and Uric Acid to the Amperometric Glucose Biosensor by Cation Exchangers Membrane and Size Exclusion Membrane. *Electroanalysis* **2005**, *17*, 2239–2245. [CrossRef]
71. Nagpal, D.; Gupta, A.; Mariappan, C.R.; Kumar, A. Mesoporous Cobalt Ferrite Flowers Based Excellent Non Enzymatic Glucose Sensor. *J. Porous Mater.* **2023**, *30*, 83–91. [CrossRef]
72. Archana, V.; Xia, Y.; Fang, R.; Gnana Kumar, G. Hierarchical CuO/NiO-Carbon Nanocomposite Derived from Metal Organic Framework on Cello Tape for the Flexible and High Performance Nonenzymatic Electrochemical Glucose Sensors. *ACS Sustain. Chem. Eng.* **2019**, *7*, 6707–6719. [CrossRef]
73. Shahnavaz, Z.; Lorestani, F.; Alias, Y.; Woi, P.M. Polypyrrole-$ZnFe_2O_4$ Magnetic Nano-Composite with Core-Shell Structure for Glucose Sensing. *Appl. Surf. Sci.* **2014**, *317*, 622–629. [CrossRef]
74. Li, Y.; Zhao, M.; Chen, J.; Fan, S.; Liang, J.; Ding, L.; Chen, S. Self-Assembled $NiFe_2O_4$/Carbon Nanotubes Sponge for Enhanced Glucose Biosensing Application. *Appl. Surf. Sci.* **2016**, *362*, 115–120. [CrossRef]

Disclaimer/Publisher's Note: The statements, opinions and data contained in all publications are solely those of the individual author(s) and contributor(s) and not of MDPI and/or the editor(s). MDPI and/or the editor(s) disclaim responsibility for any injury to people or property resulting from any ideas, methods, instructions or products referred to in the content.